Coordination of Controllers to Development of Wide-Area Control System for Damping Low-Frequency Oscillations Incorporating Large Renewable and Communication Delay

Abdulwasa Bakr Barnawi[1]

Abstract

The modern power systems incorporate high penetration of renewable is a large, composite, interconnected network with dynamic behavior. The small disturbances occurring in the system may induce low-frequency oscillations (LFOs) in the system. If the (LFOs) are not suppressed within a stipulated time, it may cause system islanding or even blackouts. Hence, it is essential to investigate the behavior of the system under various levels of disturbances and control action must be taken to damp these oscillations. The established approach to damping the LFOs is by installing power system stabilizers (PSS). PSS uses the local signals from generators to control the oscillations. The dominant source of inter-area oscillations in power systems is due to overloaded weak interconnected lines, converter-interfaced generation, and the action of the high gain exciter present in the system. Consequently, wide area control is needed to control the inter-area oscillations existent in the system. This paper developed a coordinated design of conventional PSS, static compensator, renewable converters, and wide area controller for damping the local and inter-area oscillations in renewable incorporated power systems. The performance of the developed controller is evaluated through the time domain analysis and eigenvalue analysis. A comparison of the introduced controller has been done with other standard conventional methods. The choice of input signals for the wide area controller from the wide-area measurement system is done based on the controllability index. Additionally, the location of the controller must be identified to dampen the inter-area oscillations in the system. In this paper, the controllability index is calculated to find out the highly affected wide area signals for considering it as the feedback signal to a developed controller. The location of the controller is recognized by computing the participation factor. The developed controller has experimented on renewable incorporated large study power systems when time delay and noise are present in wide area signals.

Abbreviations

AVR	Automatic Voltage Regulator
CIGs	Converter Interfaced Generations
CWAC	Coordinated Wide Area Controller
DFIG	Doubly-Fed Induction Generator
ESD	Energy Storage Device
FACTS	Flexible Alternating Current Transmission System
GPC	Generalized Predictive Control
GSC	Grid Side Converter
GW	Gigawatt
HVDC	High Voltage Direct Current
HSV	Hankel Singular Values
IAO	Inter Area Oscillation
IPFC	Interline Power Flow Controller
LDC	Local Damping Controller
LFO	Low Frequency Oscillation
LMI	Linear Matrix Inequalities
LQG	Linear Quadratic Gaussian
LTI	Linear Time-Invariant
MATLAB	Matrix Laboratory
MPPT	Maximum Power Point Tracking
MW	Megawatt
NETS	New England Test System

✉ Abdulwasa Bakr Barnawi
abarnawi@kku.edu.sa

1 Department of Electrical Engineering, College of Engineering, King Khalid University, Abha, Saudi Arabia

Springer

PCC	Point of Common Coupling
PDC	Power Distribution Centers
PLC	Programmable Logic Controllers
PMU	Phasor Measurement Unit
PSS	Power System Stabilizer
POD	Power Oscillation Damping
RES	Renewable Energy Sources
RSC	Rotor side converter
RTU	Remote Terminal Unit
SCADA	Supervisory Control and Data Acquisition
SDC	Supplementary Damping Controller
SGs	Synchronous Generators
SPV	Solar Photovoltaic
SPVGRs	Solar Photovoltaic Generation Resources
SSSA	Small Signal Stability Analysis
SSSC	Static Synchronous Series Compensator
STATCOM	Static Synchronous Compensator
SVC	Static VAR Compensator
TCPST	Thyristor-Controlled Phase-Shifting Transformer
TCSC	Thyristor-Controlled Series Capacitor
UPFC	Unified Power Flow Controller
VSC	Voltage Source Converter
VSWT	Variable Speed Wind Turbine
WADC	Wide Area Damping Controller
WAMS	Wide Area Measurement System
WECC	Western Electricity Coordinating Council
WF	Wind Farm
WGRs	Wind Generation Resources

Table 1 Incidents occurred by Low-frequency inter-area oscillations

Nations	Year(s)	Frequency of oscillation (Hz)
UK	1980	0.5
Taiwan	1984, 1989, 1990–92	0.78–1.05
Western USA/Canada	1996	0.224
Scandinavia	1997	0.5
China	2003	0.4
USA	2003	0.17
Italy	2003	0.55

1 Introduction

The state-of-the-art power system is a large and complex interconnected network with a number of components possessing nonlinear characteristics. As a consequence of rising interconnection and the use of new technologies, the complexity of the system is even more increasing. Small disturbance occurs in the system due to changes in demand, loss of generation, overloading of weak tie lines or due to high gain exciter operations. These disturbances result in the production of low-frequency oscillation (LFOs) in the system (0.1–2 Hz). Two main categories of LFOs are local and inter-area oscillations (IAOs) modes. The local mode of oscillation affects the system locally or a small part of the system. The IAOs are caused by two or more groups of coupled generating units of areas that oscillate against each other. Hence, multiple areas of power system are involved in it. In order to provide stable and reliable operation to its consumers, the system has to be modelled and the transient and dynamic performances have to be investigated under various levels

of disturbance as well as appropriate control strategies and measures have to be determined to control them [1].

Local and IAOs are LFOs that lead to small signal stability issues. It endangers the system stability, influences the power transfer capacity in power lines, and even system blackouts. Hence, it is very essential to use oscillation dampers to stabilize the power system. When a single power generating unit or a set of generators at a station swing against the rest of the system, LFOs occur. The main cause for the local mode of oscillations is high gain exciter action operation. Generally, the local mode of oscillations is in the frequency span from 1.0 to 2.0 Hz [2, 3].

1.1 Effects and Concerns of Low Frequency Oscillations

The LFOs are more poorly damped, as the number of interconnections and the energy exchanges in the electrical networks grow, raising concerns about power system stability. If no countermeasures are taken to suppress the oscillations, then system blackouts may occur as shown in [4]. A series of blackouts have occurred all over the world, due to LFOs. Some of the major blackouts are listed here. Hydro Quebec system in the Canadian province has faced blackouts, due to LFOs in the frequency of 0.6 Hz as shown in [5]. Brazil's North–South interconnection system has faced LFOs in the frequency range of 0.15 Hz, and it is shown in [6]. Indian grid faced severe blackouts and it is shown in [7]. One of the major blackouts occurred in the year 2012 and the main reason for the blackout was the overloading of power transmission lines as shown in [8]. Hence, these oscillations endanger the system stability, influence the power transfer capacity in power lines and generate system blackouts. Some other remarkable incidents [9] occurred by the IAOs LFOs are shown in Table 1.
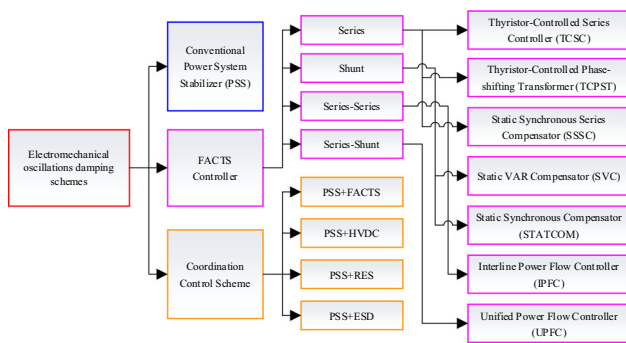
Fig. 1 Types of damping methods for LFOs

1.2 Literature Review

Due to the excessive demand of power in the grid, power systems all over the globe are constrained to operate at their stability limit. Under this scenario, high gain exciter action and overloaded interconnecting tie lines may introduce LFOs in the system. LFOs were present in the power network even in the early days of the twentieth century. A detailed study of the different types of LFOs and the nature of oscillations in the power systems is discussed by Rogers [10]. The LFOs damping approaches may be established considerably into three classes, significantly, PSS-based, flexible alternating current transmission system (FACTS)-based, and coordinated approach-based damping methods, shown in Fig. 1. Power demand has increased substantially in recent years, to meet the power demand it is essential to expand power generation and transmission. Due to limited resources for power production, environmental restrictions, and the cost of construction, the expansion of power generation and transmission becomes difficult. One of the alternatives to building new transmission lines is full utilization of the existing transmission system. The recent development of power electronics technology introduces FACTS controllers in the power system for efficient utilization of the existing transmission system.

Over the years, a significant amount of research has been directed at the damping control of LFOs in the area of power systems. To magnify the damping of LFOs (IAOs modes), supplementary damping controls of the FACTS devices are designed using eigenvalue sensitivity [11], pole-placement [12], root-locus [13], and phase-gain compensations [8] techniques. However, due to limited operating points being considered during control synthesis, the controller obtained from these approaches does not provide required damping actions at other operating conditions. To advance the robustness of the control design, $\mathcal{H}_\infty$ techniques have been employed in the power systems [14]. A systematic result of the $\mathcal{H}_\infty$ control delivers required the performance and robustness of the system with several operating states, however,

suffers from pole-zero rescission. The $\mathcal{H}_\infty$ control problems are extricated by utilizing linear matrix inequalities (LMIs) [15]. The damping controller design for PSSs by LMI approach has been shown in [16]. In [11]–[17], local signals considered as a feedback input to the damping controllers. However, due to the scarcity of global observability of the LFO modes in the local signals, the damping controllers designed by using local signals cannot confer adequate damping to the LFOs.

Recently developed WAMS technology resolves the problem of lack of global observation for the local controllers and restrain the inter-area oscillations by designing WADCs based on remote signals [18]. Various techniques in the literature have been reported for WADCs including designs for supplementary controls of generator excitation [19], FACTS [20–22] and high-voltage direct current (HVDC) devices [23–25].

The coordination control is required to avoid the other controller's effect to the power system responses. In [26] addressed the coordination work of TCSC and PSS controller in a nonlinear model of SMIB power system with GA optimizing technique and found the effective responses better than simple lead-lag PSS. In [27], the simulation work on a sequential quadratic program on three machines such as nuclear, thermal and hydro power stations considering TCSC, static voltage compensator (SVC) and PSS all into account to show the robustness and effectiveness of the overall system responses through regulating line impedance by TCSC, voltage profile by SVC and damping by PSS. In [28], proposed TCSC, SVC and PSS simultaneously tuned coordinately by adaptive velocity update relaxation particle PSO to enhance the stability and damping. In [29], investigated the robustness of the TCSC and PSS coordinated controller using optimization technique with eigenvalue shifting method.

In a coordinated wide-area control (CWAC) system, PSS, FACTS controllers, and DFIG and SPV converters are operated as an actuator to deliver the damping for LFOs modes. The phasor measurement units (PMUs) and actuators are conjoined with the CWAC via the communication system. A prevailing arrangement of CWAC accompanied by time delay is shown in Fig. 2.

The WAMSs monitoring system based on the PMUs are employed to determine the magnitude and phasors of voltage and current waveforms of the utility grid, which are stamping with time-synchronized pulses (with an accuracy of one microsecond) using GPS. Synchrophasor is a technology that came into the picture when a measurement is time-synchronized with universal time using GPS. Synchrophasor enables the synchronization and time alignment of all PMUs measurements taken at different owners or from remote locations. By combining these synchronized measurements one can produce a precise and exhaustive view of the interconnected power system. Synchrophasors facilitate the correct
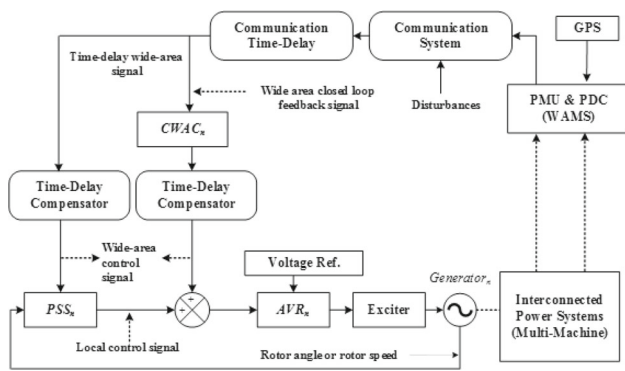
Fig. 2 Prevailing design of CWAC with time delay

information about the state of the power grid and also trigger restorative actions to preserve the reliability of the interconnections. PMU usually produces phasor information onetime in different ones or processes. Due to the rapid stimulating rate of the PMUs, they can estimate the state of the dynamical system under both steady-state and transient conditions of the power system. The measurements from the different PMUs are accumulated and transmitted to the phasor data concentrator (PDC) by employing communication links such as telephone lines, microwaves, and fiber optics. Fiber optics channels are best among all communication links due to their least total link delay. The measurements finally received by the PDC can be further utilized for both mode estimation as well as control action to ensure the stability of the power system [30]. However, the signals acquired from PMUs at controllers are with the noise and delay due to the communication process.

The examination and synthesis of delayed systems have been extensively studied over the past decade [31]–[35]. The CWAC procedure for delayed systems with saturated inputs is more complicated than the without time delay because the effectiveness of the designed CWAC for time delay systems depends on the stability of the time delay system. The global/semi-global and regional stabilization of time delay systems with actuator saturation is shown in [32]–[33]. In [34]–[35], the delay-dependent conditions are proposed for the invention of a delay compensator for a linear system.

1.3 Contributions

From the above discussion, it is observed that in WAMS technology-based control schemes, the measured signal is transmitted from PMUs to the wide-area controller with the help of a phasor data concentrator (PDC). The robust controller using the wide-area signal as feedback can deliver acceptable damping to the low-frequency IAOs modes for varying operating conditions. A simple robust controller is
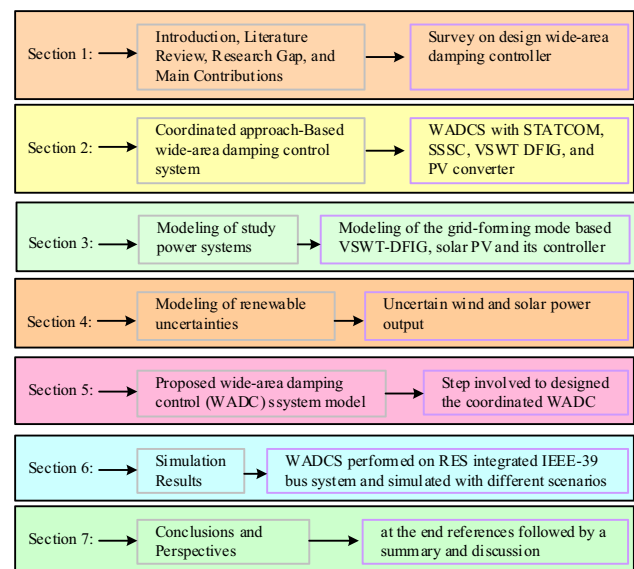

Fig. 3 Organization of paper

always desirable for wide-area control. Hence, in this paper, a simple robust CWAC is proposed for large renewable incorporated power systems. The supreme contributions of this research are highlighted-

- A robust coordinated wide-area controller (CWAC) is proposed to enhance the damping of the critically poorly damped LFOs (especially IAOs modes).
- The development of CWAC is done with the coordination of FACTS (STATCOM, and SSSC), and renewable converter (DFIG and SPV).
- The time delay is unavoidable in the wide-area signal feedback. Hence, a CWAC is suggested to mitigate the effect of time delay in the wide-area signal as well as to enhance the damping of the IAOs mode.
- This paper presents a dynamic accurate model of the renewable integrated power system for small signal analysis. A comprehensive analysis is performed to characterize the dynamic system.
- The CWAC control design is executed when communication is delayed, noise is being in the wide-area signal and implemented on the utility-scale power system incorporated DFIG wind farm and solar power generation system.

1.4 Paper Structure

The layout of the paper is shown in Fig. 3.

2 Coordinated Approach-Based CWAC

The basic operation of the generators is to generate power and transmit it through the transmission lines without interruption and maintain stability. However, the presence of system oscillations deteriorates the flow of steady-state power in the transmission line and the power system loses its stability if oscillations are not damped out at an early stage. In this work, the rotor angle stability is investigated through the auxiliary excitation control system with the coordination of a FACTS device and renewable converter for damping system oscillations. The rotor angle stability is one which maintains all the generators of power system in synchronism during pre and post disturbances. The rotor angle instability occurs due to changes in dynamics in the synchronous generator during normal or small disturbances like gradual changes in load, and power, and severe disturbances such as three-phase faults, line tripping. These disturbances create oscillations in rotor about the initial angle of rotation. During this oscillation, the kinetic energy is shared between mechanical torque and electrical torque which results in electromechanical oscillations at low-frequency. The oscillations may occur in a generator with respect to other generators in one area which is known as local mode oscillations or a group of generators in one area oscillating with other groups of generators in another area which is called as inter-area mode oscillations. The existence of these LFOs decreases the steady power flow in the transmission line and makes all power system variables oscillate and persist which may lead to cascade outage of the entire power systems. If sufficient damping measures are not taken into account, it brings rotor angle instability and this motivates the present work. In this paper, the system damping and the power system stability have been improved by designing the CWAC to modify the characteristics of system responses. The STATCOM FACTS device is employed with the coordination of CWAC for effective damping and enhancing the stability simultaneously. The simplified block illustration of the CWAC as coordination of STATCOM, SSSC, and converter of variable speed based wind turbine doubly fed induction generators, and solar converter is shown in Fig. 4.

3 Modeling of Study Power Systems

The NETS test system, shown in Fig. 5, consists of 10 generating units (SGs) and 39 buses, where static excitation and local damping controllers are mounted with G_2 to G_9. G_{10} is an analogous study unit that takes the system data from [36]. The generation system is sixth order, first order exciter and 3rd order local damping controller. In the revised NETS system, the wind farm consists of multiple DFIG sets linked to bus #17. A 111 *MVA*, 100 MW solar power generating
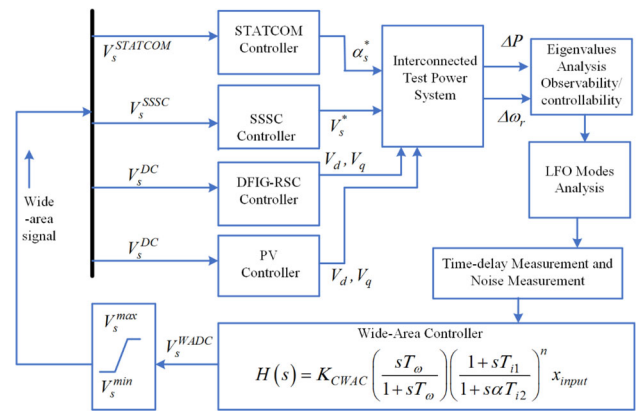

Fig. 4 Coordinated design and its block model representation of WADC, FACTS, and renewable converter

system (SPV) is linked to bus #16. For reactive power aid, STSTCOM is installed on bus #17. For extra damping support, SSSC is linked between buses #16 and #17. The power system dynamics are essentially required for modeling and to know the system stability. The basic reasons of power system dynamics change with power demand and causes of various disturbances. The behavior of the negative damping torque is analyzed through characteristic equations of the NETS system model [37].

Figure 6 shows the excitation system of the generator which contains exciter and AVR. The classical model is taken where the field flux is constant. The change in mechanical torque due to slow response is neglected. The second-order linearized model is developed following a small perturbation and is expressed in two first-order form [2] as,

$$\frac{d\delta}{dt} = \omega \tag{1}$$

$$\frac{d\omega}{dt} = \frac{1}{M}\left\{T_{em} - (i_i i_q + \Psi_q i_d) - \omega D\right\} \tag{2}$$

$$\frac{dE'_q}{dt} = \frac{1}{T'_{d0}}\left\{-E'_q + E_{fd} - (x_d - x'_d)\right\} \tag{3}$$

$$\frac{dE'_d}{dt} = \frac{1}{T'_{q0}}\left\{-E'_d - i_q\left(x_q - x'_q\right)\right\} \tag{4}$$

where, D is the damping coefficient due to damper winding in rotor in p.u., ω is the angular speed of rotor in p.u., T_{em} is torque in p.u., and δ is rotor angle (in elec.rad). Each generating unit in the system is linked with a PSS, consists-phase shift blocks, shown in Fig. 7.

The loads and transmission network are modeled algebraically by their admittance matrices. All loads are considered to be constant impedance loads. These loads are static loads where power directly varies with the square of the voltage magnitude. The load admittance matrix Y_L is defined
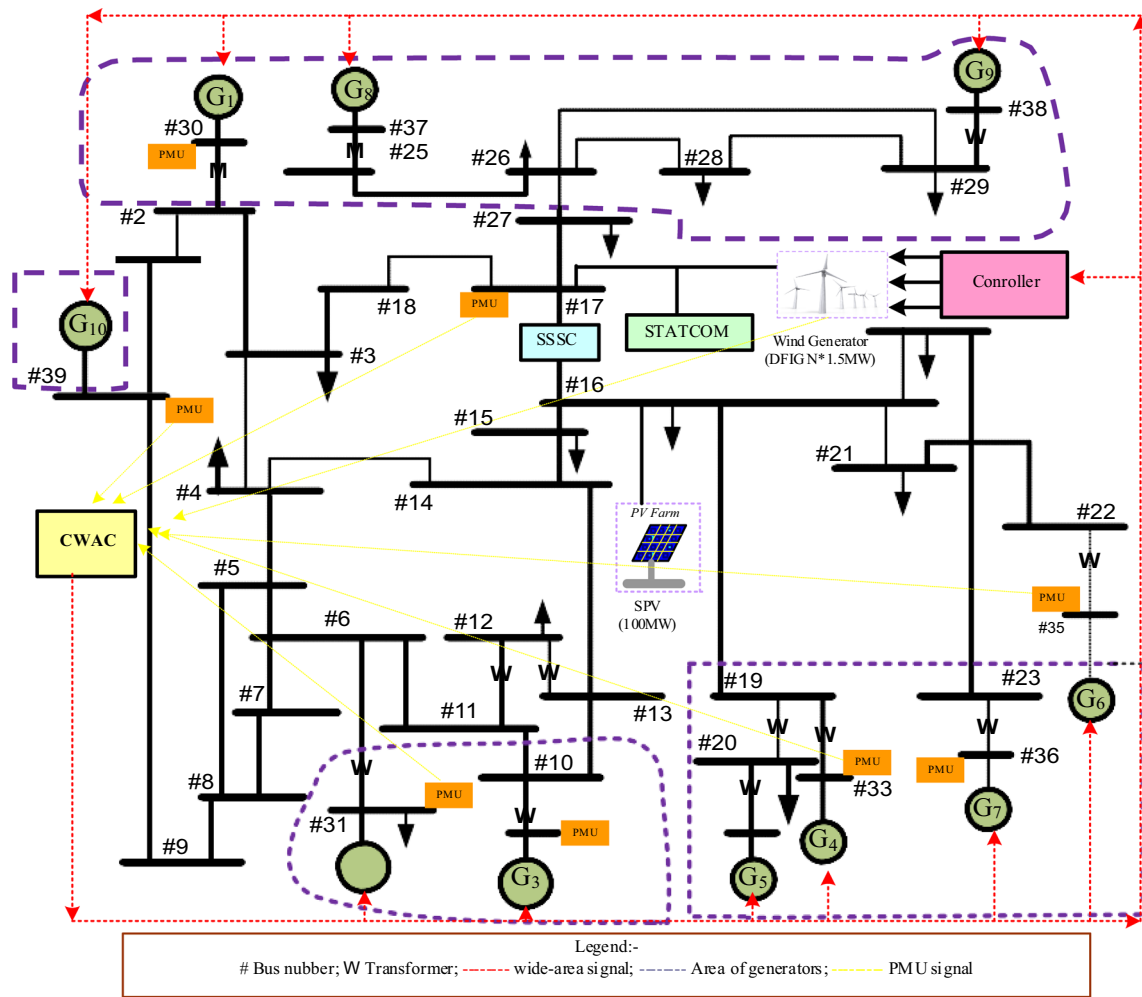
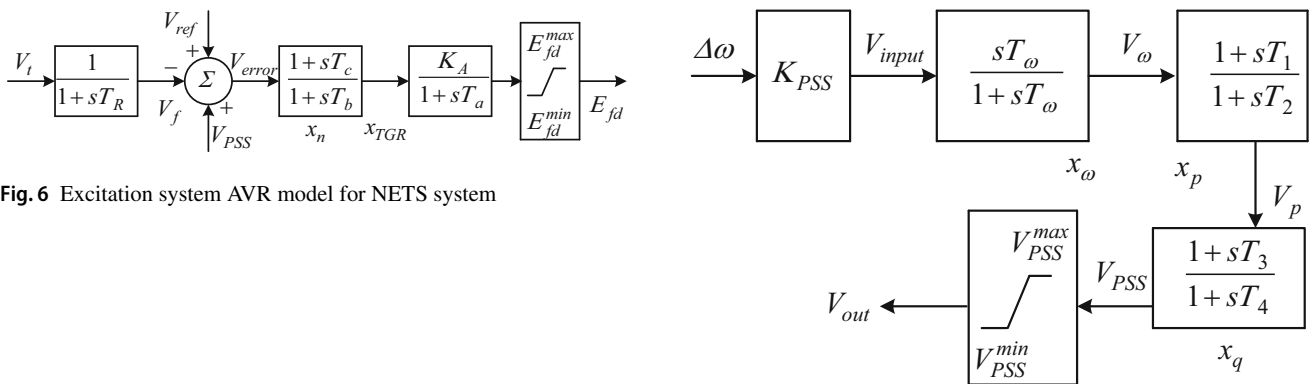**Fig. 5** Modified IEEE NETS system with CWAC

Fig. 6 Excitation system AVR model for NETS system

Fig. 7 Local damping controller, PSS model

as the load model. A transmission network is presented by lumped parameters and modeled algebraically by its admittance matrix Y_N. This matrix is formulated by using the line impedances. The augmented admittance matrix Y_{aug} in an interconnected power system along with generator admittance matrix Y_G is shown as $Y_{aug} = Y_N + Y_L + Y_G$. The augmented admittance matrix Y_{aug} relates the terminal voltage and current vectors in the complex domain.

3.1 Wind Generation System Modeling

Globally, energy is an emerging renewable energy resource. Using appropriate equipment, wind energy is effectively transformed into electrical energy [40]. The modelling of

a wind power generation system is critical for successful hybrid energy system planning. On-site appearances, load demand, meteorological data, and economic data are the most important factors in wind energy system modeling. The load demand, various wind statistics, and input data are used to construct a mathematical analysis and model for wind turbines [41]. A number of factors influence wind turbine power production. As mentioned in the literature, these criteria might be dependent on internal strategy or external atmospheric conditions. The parameters relating to optimal power production at minimal wind speed for the specified location should be considered, while choosing a wind turbine [42]. To meet the parameters of an AC system, the wind turbine needs a very complex control system. Wind generator performance characteristics vary depending on location and settings [43]. The current study employs a utility-scale wind power system that is adequate for average wind availability as a result, the component's mathematical modeling becomes more important. A wind turbine with a 1.5-MW rated producing capacity is evaluated to run the suggested proposed model. The power generated by a wind turbine may be calculated using the following formula [40]-

$$p_w = \frac{1}{2}\left(\pi r^2\right)\rho C_p(\beta,\,\lambda)\omega_w^3 \; [watt] \qquad (5)$$

Here, P_{wind} is the wind power, ρ is the air density (m^3); ω_{wind} is the wind speed (m/sec); r is the radius of the turbine; $c_p(\lambda)$ is the coefficient of the power, λ is tip speed ratio and pitch angle β. Grid-forming variable speed wind generators allow rugged performance interlocked with broadly inadequate power grids. VSWT-DFIG (class-3) with controllers are shown in Fig. 8. The control loops for the rotor side and grid side converter of the wind generating units are shown in Fig. 8.

3.2 Solar PV Generation Modelling

The prevailing active benchmark created by WECC [38] for grid-connected SPV generation operated with NETS system is shown in Fig. 9. The SPV power system with regulators is shown in Fig. 10. Solar PV systems generate electricity from sunlight by using the photovoltaic effect. When semiconducting materials are exposed to light, they generate voltage and current. Electrical characteristics of solar cells alter in response to light, and this property of solar cells has been exploited for real-world applications. Depending on the desired value of voltage/current, series or parallel connections are made between the panels. PV cells are made up of polycrystalline or monocrystalline silicon. Commercially these are available as solar module or solar panel which basically is group of solar cells crammed into
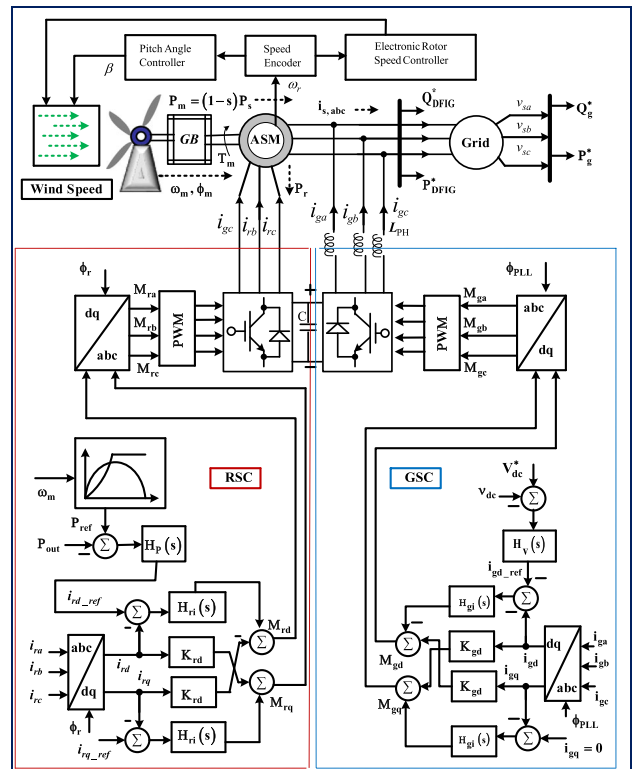

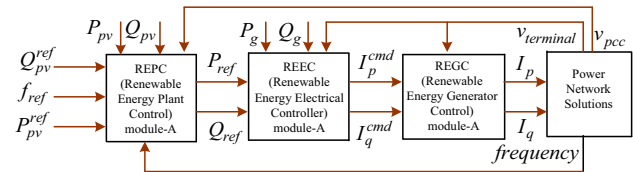**Fig. 8** VSWI-DFIG (class-3) power model with controlling

Fig. 9 SPV power generation prototype

a metal frame. In a PV system, the solar panel receives sunlight and converts incident photons into electrical energy. As PV is an unregulated dc power source, DC to AC conversion in required for usage of power in day-to-day applications. Thus, solar inverter becomes an integral part of the system. The maximum power point technique tracks and captures the maximum energy possible. This work uses solar photovoltaics for hybrid energy production. Therefore, the mathematical modelling of the solar PV component becomes more relevant. The characteristics data of the considered polycrystalline SPV array are shown in Table 4. The fundamental cell temperature and irradiance dependent equation are used to calculate the output power of a PV generator. SPV system's power output can be shown as follows [44].

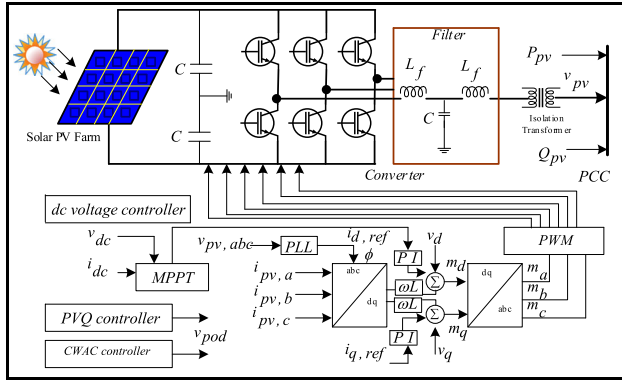$$P_{SPV} = \text{P}_{SPV,\,R}\,f_{SPV}\left(\frac{G}{G_{ref}}\right)\left[1 + 0.001 * \alpha_p(\theta_{cell} - \theta_{cell,\,ref})\right] \quad (6)$$

Fig. 10 General framework of solar PV farm with different controllers

Fig. 11 Control process of SPV system

The control strategy of PV generation is shown in Fig. 11 [39].

To calculate the output power of a PV generator, we use the actual temperature and irradiance dependent equation.

$$P_{su}(t) = P_{re}(t) \times f_{dr} \times \left(\frac{S_g}{S_{st}} \right) \tag{7}$$

$$\eta = \eta_{ref} \left[1 + 0.001 * \alpha_p \left(\theta_{cell} - \theta_{cell,ref} \right) \right] \tag{8}$$

Here, the following equations are used to calculate the fluctuation in cell temperature during daylight hours.

$$\tau \alpha_a G = \eta G + U \left(\theta_{cell} - \theta_{amb} \right) \tag{9}$$

$$\theta_{cell} = \theta_{amb} + G \left(\frac{\tau \alpha_a}{U} \right) \left(1 - \frac{\eta}{\tau \alpha_a} \right) \tag{10}$$

The value of $\tau \alpha a$ is taken as 0.8. However, at nominal operating cell temperature with no load, the efficiency of the SPV generator can be treated as zero. Therefore, applying mathematical approximation, the expression can be shown as.

$$\frac{\tau \theta_a}{U} = \frac{\left(\theta_{cell,Noct} - \theta_{amb,Noct} \right)}{G_{Noct}} \tag{11}$$

Using above equations, the modified expression of the cell temperature of the SPV generator can be given as.

$$\theta_{cell} = \theta_{amb} + \frac{G}{G_{Noct}} \left(\theta_{cell,Noct} - \theta_{amb,Noct} \right) \left(1 - \frac{\eta}{\tau \alpha_a} \right) \tag{12}$$

The voltage and current of the SPV system are shown as follows-

$$v_{pvg} = \frac{N_s \eta K^{bZ} T}{q_e} \ln \left\{ \frac{\frac{N_P I_{sc} I_r}{100} - I_{pvg}}{N_P \times I_\circ} \right\} \tag{13}$$

$$I_{pvg} = I_{sc}(G) - N_P \times I_\circ \left[\exp \left\{ \frac{(v_{array} + I_{pvg} R_s) q_e}{\eta N_s K^{bZ} T} \right\} - 1 \right] \tag{14}$$
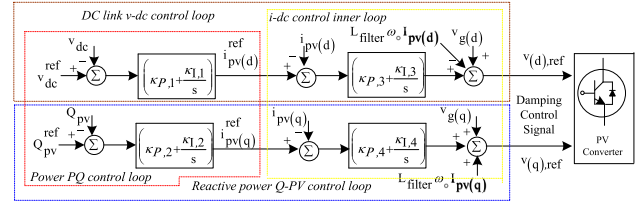
4 Modeling of Renewable Uncertainties

The unreliable characteristics of most renewable energy sources become a task for the electrical organization, which needs to answer deviations in the load demand by sending power from thermal power stations. In this section, the uncertain nature of wind, and solar are considered. The wind speed is highly uncertain in nature; different models were developed that considered the stochastic nature of wind speed. The most used model is the Weibull distribution. In the case of solar PV systems to investigate the features of solar irradiation lognormal probability density function is used [45]. Wind unit output power $P_{W,k}$ (MW) of kth wind unit corresponding to wind speed ω_W can be shown as [46]-

$$P_{W,k} = \begin{cases} 0; & \omega_W < \omega_W^{\mathcal{I}} \& \omega_W \geq \omega_W^o \\ \left(\frac{\omega_W - \omega_W^{\mathcal{I}}}{\omega_W^R - \omega_W^{\mathcal{I}}} \right) \left(P_{W,k}^R \right); & \omega_W^{\mathcal{I}} \leq \omega_W, < \omega_W^R \\ P_{W,k}^R; & \omega_W^R \leq \omega_W < \omega_W^o \end{cases} \tag{15}$$

Here, cut-in, rated and cut-out wind speed define by $\omega_W^{\mathcal{I}}$, ω_W^R & ω_W^o in m/ sec , respectively.

The solar PV output power $P_{SPV,k}$ is shown by following equation for irradiation Z_{SPV} [47]-

$$P_{SPV,k} = \begin{cases} P_{SPV,k}^R \times \frac{(Z_{SPV})^2}{Z_{SPV}^{St} \times Z_{SPV}^C}; & \left(0 < Z_{SPV} < Z_{SPV}^C \right) \\ P_{SPV,k}^R \left(\frac{Z_{SPV}}{Z_{SPV}^{St}} \right); & \left(Z_{SPV} \geq Z_{SPV}^C \right) \end{cases} \tag{16}$$

Here, Z_{SPV}^{St}, $P_{SPV,k}^R$ is defined the standard solar irradiation and rated power of kth solar PV unit. Z_{SPV}^C is a certain irradiance select as 180 w/m^2.

5 Proposed Coordinated Wide Area Control Model
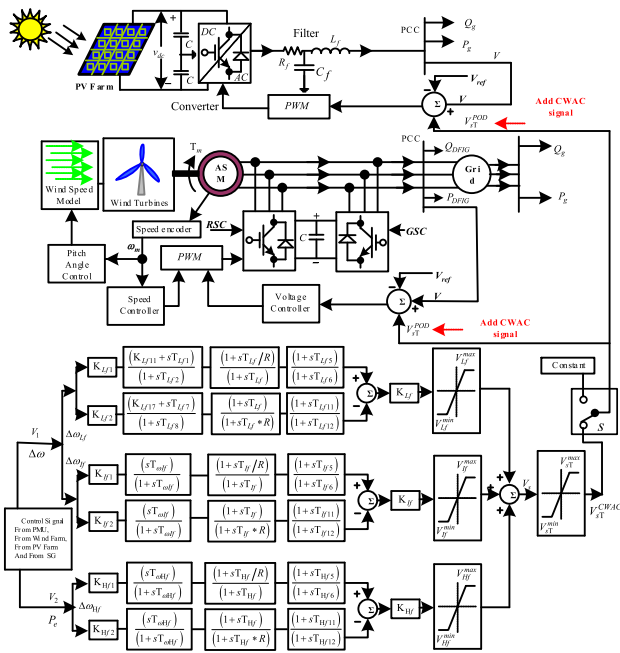
The proposed CWAC model is shown in Fig. 12. In this model

Fig. 12 The CWAC model, coordination of DFIG and SPV

Mode No.	Eigenvalues ($\lambda = \rho \pm j\omega$)
Mode #1 →	$-2.553 + j10.566$
Mode #2 →	$-1.8494 + j10.028$
Mode #3 →	$-1.5817 + j8.5503$
Mode #4 →	$-2.5633 + j8.6706$
Mode #5 →	$-1.8626 + j7.4388$
Mode #6 →	$-1.3118 + j7.1081$
Mode #7 →	$-1.8437 + j7.0812$
Mode #8 →	$-1.523 + j6.3180$
Mode #9 →	$-2.9563 + j2.5076$

speed transducers or speed synthesis are used for different frequency band (low, intermediate, and high band).

Usually, the value of R is set as 1.2; K_{lf1}, K_{lf2}, K_{if1}, K_{if2}, K_{Hf1}, K_{Hf2} are set as 66; $V_{sT}^{\min}$ & $V_{sT}^{\max}$ is set as -0.1 & $+0.1$; other undefined parameters are set 0. Limiter $V_{lf}^{\min}$ & $V_{lf}^{\max}$ is -0.04 and $+0.08$, respectively; $V_{if}^{\min}$ & $V_{if}^{\max}$ is -0.6 and $+0.6$, respectively; $V_{Hf}^{\min}$ & $V_{Hf}^{\max}$ is -0.6 and $+0.6$, respectively; K_{lf}, T_{lf}, & f_l is 20.4, 1.245, & 0.118, respectively; K_{if}, T_{if}, & f_i is 40, 0.28644, & 0.516, respectively; K_{Hf}, T_{Hf}, & f_H is 86, 0.0121, & 12.10, respectively; $T_{\omega lf}$, & $T_{\omega Hf}$ is 1 and ∞, respectively; T_{Hf5}, T_{Hf6}, T_{Hf11}, & T_{Hf12} is 0.1588, 0.0606, 0.1578, & 0.0602, respectively. The exclusive procedure and stages detailed to develop a presented control model are shown in Fig. 13.

6 Simulation Results and Discussion

The electromechanical LFOs modes are obtained of NETS power system is given below as

The nonlinear model shown using step 1 Fig. 13 is linearized around a nominal point of operation. The different local and IAO modes can be extracted from the SSSA. The linearized model came as 93th. To obtain the measurements from PMUs, the simulations are set to produce generator rotor angle and speed at 100 samples per second. The LFO modes obtained from the modal analysis, the three IAO modes are present. Here, *Mode* #6 and *Mode* #7 have poor damping. Our primary concern is therefore *Mode* #6 and *Mode* #7 i.e. $-1.3118 + j7.1081$ and $-1.8437 + j7.0812$.

Mode shape and value of participation factors for IAO *Mode* #6 is shown in Fig. 14 and Fig. 15, respectively. For this IAO mode, G_{10}, and G_2 is highly influenced and need the damping control. The inter-area's G_{10} oscillate against G_2 and G_8. The proposed damping controller location is G_{10} and G_2 can be selected for damping control. Figure 16 shown the eigenvalues for higher *4th* order model of generators, respectively with damping controller at different location. In this work, higher fourth order model is used for proposed CWAC with operational uncertainties and communication time delay and noise. SSSA outcomes (eigenvalues, frequency, and damping ratio) are shown in appendix Table 5.

Mode shape and dominant generators (greatest participation value) for IAO *Mode* #7 is shown in Fig. 17 and Fig. 18, respectively. It is clearly indicated that the generator G_5 is highest participate rotor speed state and oscillate against G_6 and G_7. Another generator's effect is negligible according to Fig. 18, so the recommended damping controller is equipped with G_4, G_5, G_6, and G_7 for damping control.

6.1 Case Study

The CWAC controller design strategy is executed in a more complex RESs, and FACTS incorporated a revised NETS system, Fig. 5. In this system, an SPV farm (rated capacity 100 MW), and a WGR farm (rated capacity 700 MW) are

Step - 1: → *Linearization and Eigenvalues Analysis*

The linearized state-space model of the system is evolved utilizing the linearization tool (MATLAB)

$\Delta \dot{x} = A\Delta x + B\Delta u$; $\Delta y = C\Delta x + D\Delta u$

Then eigenvalue (λ_i) analysis are used to

(a) Realize the critical LFO modes, (b) Choose optimal control inputs such as rotor speed ω_r, rotor angle ϕ_r, voltage and power reference

Step - 2: → *Find the input / output pair of CWAC*

Joint Controllability/Observability methos is used $\quad m_{ci} = \dfrac{\left| B^T . \psi_i \right|}{\|\psi_i\| . \|B^T\|}$ and $m_{oi} = \dfrac{\left| \phi_i . C \right|}{\|\phi_i\| . \|C\|}$

m_{ci} & m_{oi} geometrical controllability and observability measures associated with i^{th} mode, ϕ_i & ψ_i are right and left eigenvectors, corresponding to i^{th} mode. The large value of joint controllability/observability is $m_{oci} = m_{ci} . m_{oi}$ indicating that i^{th} mode is effective

→ Then choose appropriate control signals and control loop for CWAC

Step - 3: → *Wash - out filter and the phase compensator*

- The phase compensator of CWAC are selected utilizing a residue-based method

- The residue R_{ij} allied with an eigenvalue λ_i and a feedback transfer function $f_j(s, K_j)$, $\dfrac{\partial \lambda_i}{\partial K_j} = R_{ik} \dfrac{\partial f_j(s, K_j)}{\partial K_j}$,

where K_j is static gain, varies with i^{th} eigenvalue is $\Delta \lambda_i = R_{ij} H_j(\lambda_i)$, H_j is the transfer function of a feedback damping controller

- The local damping controller location is selected at j^{th} machine having the maximal value of residue R_{ij} for i^{th} LFO mode with the eigenvalue λ_i.

- The CWAC is designed with the necessary phase lead compensation $\theta_{ij} = 180 - arg(R_{ij})$ for the ith

LFO mode, therefore eigenvalue is measured by $\Delta \lambda_i = \Delta \rho_i + j\Delta \omega_i = K_j \left\{ Re(R_{ij}) + img(R_{ij}) \right\}$,

so the maximal residue for LFO mode, the input signal of CWAC is always rotor speed ω_r and selected with maximal controllability-observability.

Step - 4: → *CWAC Controller Gain* (K_{CWAC})

After the selected of the washout & phase compensator, the CWAC gain (K_{CWAC}) is tuned to get the optimal damping for the LFO mode $(K_{CWAC}$ varies from 0 to 150$)$; $K_{CWAC} = 150$, high damping factor is obtained for the LFO mode.

Step - 5: → *Determine delay margin for multiple time − delay with gain* K_{CWAC} *of reduced order model*

The feedback linearized model of the reduced order system with communication latencies is given by

$\begin{cases} \dot{X}_{redo}(t) = \hat{A}_{redo} X_{redo}(t - \tau_d) + \hat{B}_{redo} u_{redo}(t - \tau_d) \\ y_{redo}(t) = \hat{C}_{redo} X_{redo}(t - \tau_d) + \hat{D}_{redo} u_{redo}(t - \tau_d) \end{cases}$; $(\tau_d > 0)$ is the universal time delay $(\tau_d) = \tau_a + \tau_c + \tau_y$

Feedback-loop linearized DE is determine using $\dot{X}_{redo}(t) = \hat{A}_{redo} X_{redo}(t) + \sum_{\ell=1}^{v} \hat{A}_{redo}^{\ell} X_{redo}^{\ell}(t - \tau_d^{\ell})$

Where, $v = 1, 2, \dots n$ (multiple delay) is adopted as $e^{\eta t} v$; such as $det \Delta(\eta) = 0$; $\Delta(\eta) = \eta I_n - A_0 - \sum_{\ell=1}^{v} \hat{A}_{redo}^{\ell} e^{-\eta \tau_\ell}$

$$\hat{A}_{redo} = \begin{bmatrix} \hat{A}_r & \hat{B}_{r1}\hat{C}_{s1} & \hat{B}_{r2}\hat{C}_{s2} & \dots & \hat{B}_{rm}\hat{C}_{sn} \\ O_{3\times r} & \hat{A}_{s1} & O_{3\times 3} & \dots & O_{3\times 3} \\ O_{3\times r} & O_{3\times 3} & \hat{A}_{s2} & \dots & O_{3\times 3} \\ \vdots & \vdots & \vdots & \vdots & \vdots \\ O_{3\times r} & O_{3\times 3} & O_{3\times 3} & \dots & \hat{A}_{sn} \end{bmatrix} ; \quad \hat{A}_{redo}^{\ell} = \begin{bmatrix} \hat{B}_{r\ell}\hat{D}_{s\ell}\hat{C}_{s\ell} & O_{r\times 3n} \\ O_{3(\ell-1)\times r} & O_{3(\ell-1)\times 3n} \\ \hat{B}_{r\ell}\hat{C}_{s\ell} & O_{3\times 3n} \\ O_{3(n-\ell)\times r} & O_{3(n-\ell)\times 3n} \end{bmatrix}$$

Lyapunov function for communication latencies to design CWAC is presented in follwing equation

$$v(t) = \chi^{\dagger}(t) P \chi(t) + \left[\sum_{\ell=O}^{v-1} \left\{ \int_{t-\tau_{\ell+1}}^{t-\tau_\ell} \chi^{\dagger}(s) Q_{\ell+1} \chi(s) ds + (\tau_{\ell+1} - \tau_\ell) \right\} \right] \times \left[\sum_{\ell=O}^{v-1} \int_{-\tau_{\ell+1}}^{-\tau_\ell} \left\{ \int_{t+\phi}^{t} (\hat{\chi}^{\dagger}(s) R_{\ell+1} \hat{\chi}(s) ds d\phi \right\} \right]$$

In CWAC, for diffrent latencies, delay margin is determined by utilizing the stability benchmark and approximating it by Pade

approximation. The delay margin is calculated for the different gains K_{CWAC} of $\tau_d^{CWAC} = \sqrt{\left(\tau_{d1}^{CWAC}\right)^2 + \left(\tau_{d1}^{CWAC}\right)^2}$ & $\phi = \arctan\left(\dfrac{\tau_{d1}^{CWAC}}{\tau_{d2}^{CWAC}}\right)$

Step - 6: → *Proposed cordinated CWAC tested on Large power system* $(Simulation results)$-

The CWAC control design is executed when communication is delayed, noise is being in the wide-area signal and implemented on the utility-scale power system incorporated DFIG wind farm and solar power generation system.

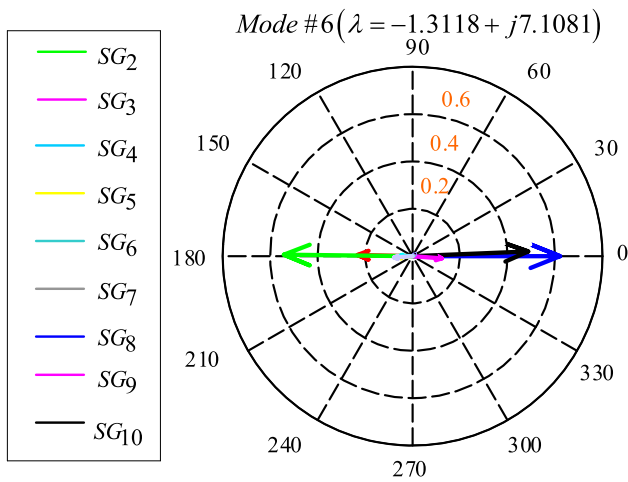**Fig. 13** Phase applied to develop the CWAC

$Mode \#6(\lambda = -1.3118 + j7.1081)$
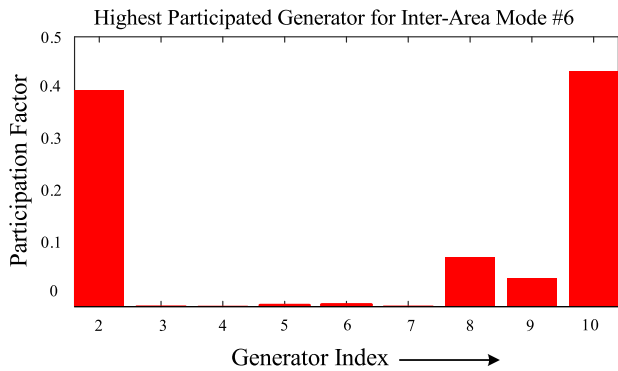
Fig. 14 Mode shapes for IAO *Mode* #6

Fig. 15 Dominant generators for IAO *Mode* #6

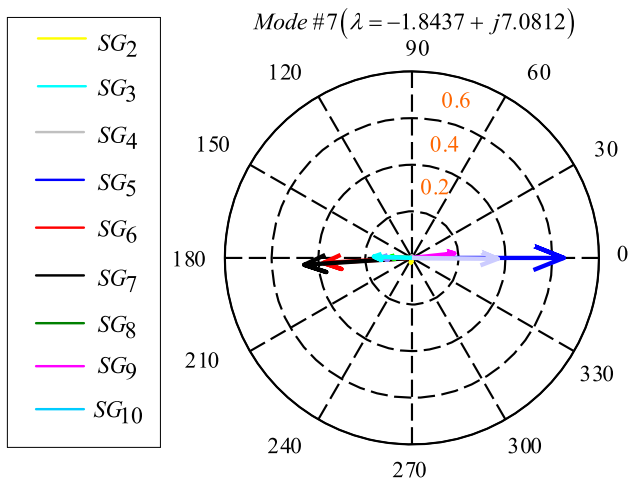$Mode \#7(\lambda = -1.8437 + j7.0812)$

Fig. 16 Mode shapes for IAO *Mode* #7

linked at bus#16, and bus#17, respectively. A series FACTS device SSSC is coupled amidst bus#16 and bus#17. A STATCOM is linked with bus#17. The complete description of
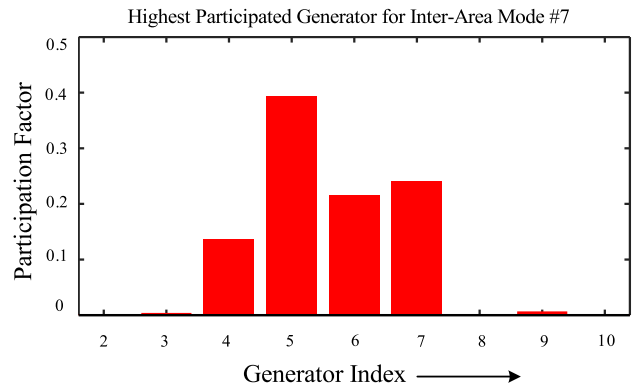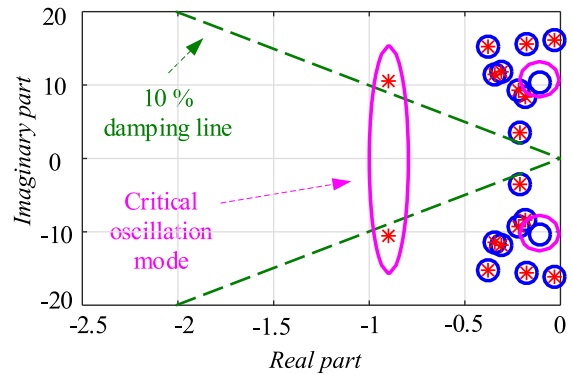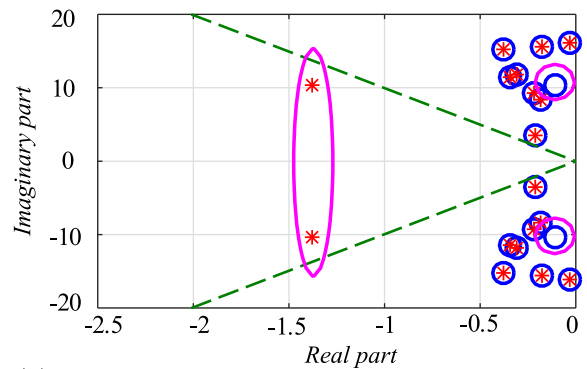
Highest Participated Generator for Inter-Area Mode #7

Fig. 17 Dominant generators for IAO *Mode* #7

(a) Eigenvalues depiction with damping control at G_5.

(b) Eigenvalues depiction with damping control at G_7 & G_5.

Fig. 18 Eigenvalues with/without CWADC

the system is already given in Sect. 3. The nonlinear system is linearized around an operating condition in MATLAB and 108th order linear plant is found. Three critical LFO IAO modes are discovered from the SSSA of the system (*Mode* #1; *Mode* #2; *Mode* #3). Therefore, the principal ambition is to enhance the damping for IAO modes. The active power flow is utilized as the feedback control signal for the controller. The geometric controllability and observability indices concerning IAO modes are computed to obtain

Table 2 Operating scenarios

Scenario	Communication effects	Description
Scenario-1	$\tau_{d,1} = 0$ sec	No disturbance ($0 \le t < 1$); 3-φ fault between bus#16 and bus#17 ($1 \le t \le 10$)
Scenario-2	$\tau_{d,2} = 0.2$ sec	No disturbance ($0 \le t < 1$); 3-φ fault between bus#16 and bus#17 ($1 \le t \le 10$)
Scenario-3	$\tau_{d,3} = 0.5$ sec	No disturbance ($0 \le t < 1$); 3-φ fault between bus#16 and bus#17 ($1 \le t \le 10$)
Scenario-4	$\tau_{d,4} = 0.75$ sec	No disturbance ($0 \le t < 1$); 3-φ fault between bus#16 and bus#17 ($1 \le t \le 10$)
Scenario-5	$\tau_{d,3} = 0.5$ sec	No disturbance ($0 \le t < 1$); 3-φ fault between bus#13 and bus#14 ($1 \le t \le 10$)
Scenario-6	$\tau_{d,2} = 0.2$ sec	No disturbance ($0 \le t < 1$); 3-φ fault between bus#13 and bus#14 ($1 \le t \le 10$)
Scenario-7	Noise	No disturbance ($0 \le t < 1$); 3-φ fault between bus#16 and bus#17 ($1 \le t \le 20$)

the most promising location of CWAC. The generator which has the larger controllability index value concerning the most critical IAO mode and a smaller controllability index value concerning other IAO modes is considered the best location to locate the CWAC. G_5 is found as the best controller location. Similarly, it is observed that the active power flow through transmission line 21 (Active power flow through bus#12 to bus#13) has the largest geometric observability index value with respect to inter-area *Mode* #1 and also a smaller geometric observability index value with respect to *Mode* #2, and *Mode* #3. Hence, P_{12-13} is used as the considerable stabilizing control signal for the CWAC. For simulation and evaluate the performance of CWAC, the diverse operating scenarios are shown in Table 2. Real-time simulators are used to verify the simulation findings, which were produced via MATLAB.

A communication network is required to send wide-area signals from outlying locations to the control center. The use of a communication network causes the feedback loop to experience time delays. In power systems, time delays are inevitable, and it is well-recognized that they can cause performance deterioration, oscillations, and possibly closed-loop instability [48]. The length of time delays normally ranges from tens to several milliseconds and depends on the communication network, the type of protocol being used for transmission, and the signal transfer distance. Therefore, it is crucial to take time delays into account throughout the CWAC design process and identify the greatest upper bound

of time delay, or the delay margin, below which the power system is able to maintain stability. Based on whether or not the stability requirements depend on the size of the delay, the time delay stability analysis has been divided into two categories: delay-independent and delay-dependent. In contrast to the adequate circumstances in the delay-dependent stability analysis, which depends on the upper bound of the delay, the sufficient conditions in the delay-independent stability analysis are independent of the duration of the delay.

In this work, the performance of CWAC is assessed considering four different magnitudes of time delay (τ_d), $\tau_{d,1} = 0$ sec, $\tau_{d,2} = 0.2$ sec, $\tau_{d,3} = 0.5$ sec, and $\tau_{d,4} = 0.75$ sec.

The responses of CWAC to various time delays in terms of the rotor angle of machine G_5, G_6, and G_7 are shown in Fig.. 19. Figure 19 shows what happens when no control measures are used to stabilize the system after a significant disturbance: the angle oscillations increase. Additionally, it appears that when delays grow, oscillations grow as well. In scenario-1, time delays are not taken into account, but a 3-φ fault is introduced at $t = 1$ sec between buses #16 and #17 with a fault period of $100\,m$ sec. Scnerio-1 responses are shown in Fig. 19a,b,c. These simulated results show that the advised CWAC efficiently mitigates IAOs. Oscillations stop using the suggested controller in less than 3 s, which is acceptable. In scenario-2, time delays $\tau_{d,2} = 0.2$ sec are considered, and a 3-φ fault with a $100\,m$ sec fault duration is introduced between buses #16 and #17 at time $t = 1$ sec. In Fig. 19a,b,c, the Scnerio-2 responses are shown. These simulated results demonstrate that the recommended CWAC effectively reduces both the effect of time delays and IAOs. Scnerio-3 responses are given with time delay $\tau_{d,3} = 0.5$ sec, and 3-φ fault. Responses from Scnerio-4 include a time delay $\tau_{d,4} = 0.75$ sec, and a 3-phase fault. The comparative damping ratio of IAO modes obtained from different control methods are shown in Table 3. The CWAC offers enough dampening for LFO IAO modes following a 3-phase fault and time delays.

Fig. 20 displays the voltage responses using CWAC at various buses. According to the simulation findings, the suggested CWAC is successfully operating in the RESs incorporated system. The time delay $\tau_{d,3} = 0.5$ sec, and a 3-φ fault with a $100\,m$ sec fault duration is introduced between buses #16 and #17 at time $t = 1$ sec are taken into account in order to produce the voltage responses with CWAC. The voltage responses at PCC SPV bus#16, PCC DFIG bus#17, and bus#13 are shown in Fig. 20a,b,c, respectively. With the CWAC, voltage oscillations are reduced.

Another monitoring variable to verify the effectiveness of the specified CWAC is the deviation of the active power transfer in the tie-line. The active power deviation response for $\tau_{d,2} = 0.2$ sec, $\tau_{d,3} = 0.5$ sec delays are shown in Fig. 5 and Fig. 21a,b. When a 0.2-s delay in the wide-area signal is taken into account, replies show that CWAC operate

Table 3 Comparisons of different controller in terms of damping ratio of IAO modes

Control ↓	Mode #1		Mode #2		Mode #3	
	$f(Hz)$	ξ	$f(Hz)$	ξ	$f(Hz)$	ξ
No Control	0.4339	0.1282	0.5725	0.1896	0.7182	0.1474
Only PSS	0.4202	0.1953	0.5943	0.1982	0.7302	0.1765
Lead-lag WADC	0.4154	0.2414	0.6415	0.2014	0.9536	0.1965
With CWAC (No delay)	0.4963	0.7654	0.5473	0.9321	0.8962	0.8985
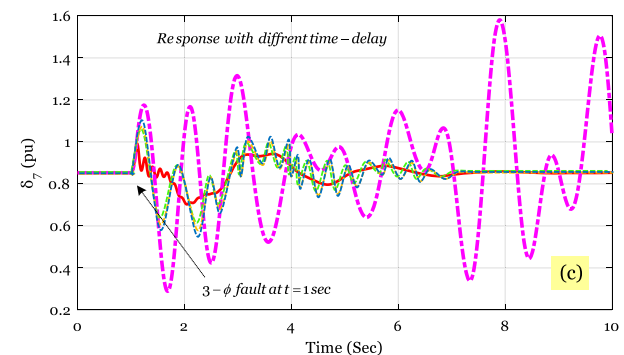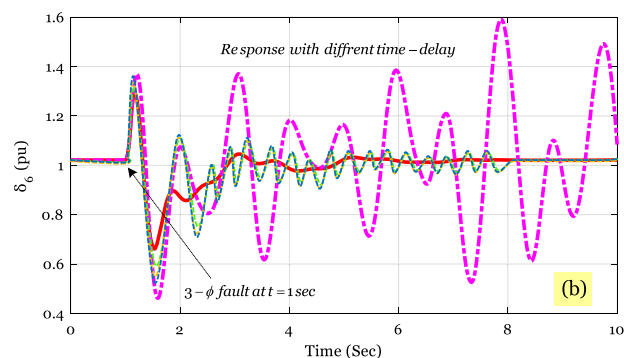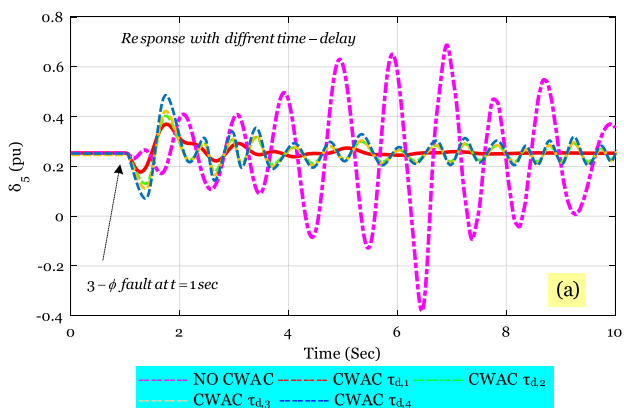
Fig. 19 Response of CWAC with different time delay, **a** G_5 rotor angle (δ_5) pu; **b** G_6 rotor angle (δ_6) pu; **c** G_7 rotor angle (δ_7) pu
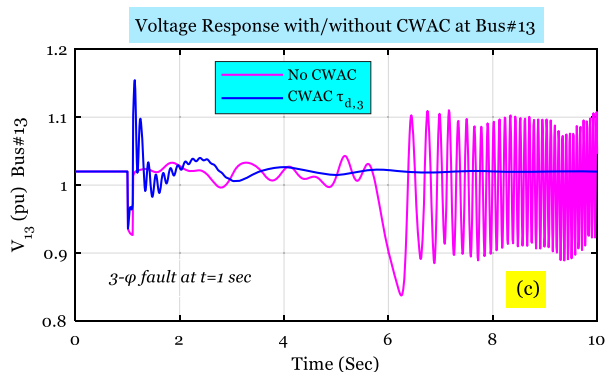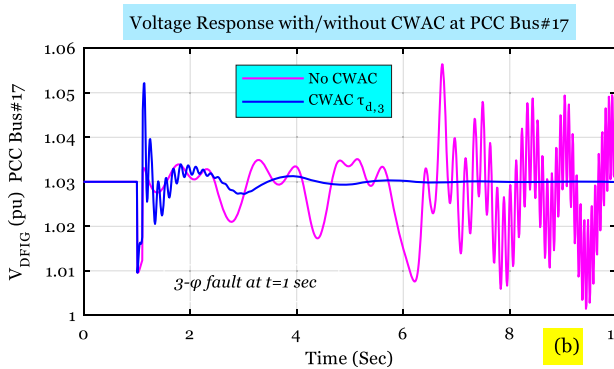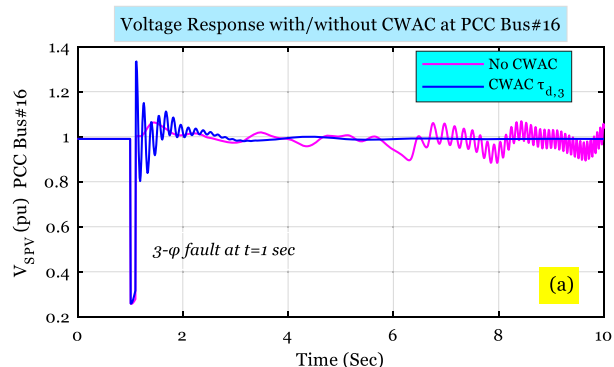

Fig. 20 Voltage response of CWAC with $\tau_{d,3} = 0.5$ sec, **a** at SPV bus#16 in pu; **b** at DFIG bus#17 in pu; **c** at bus#13 in pu
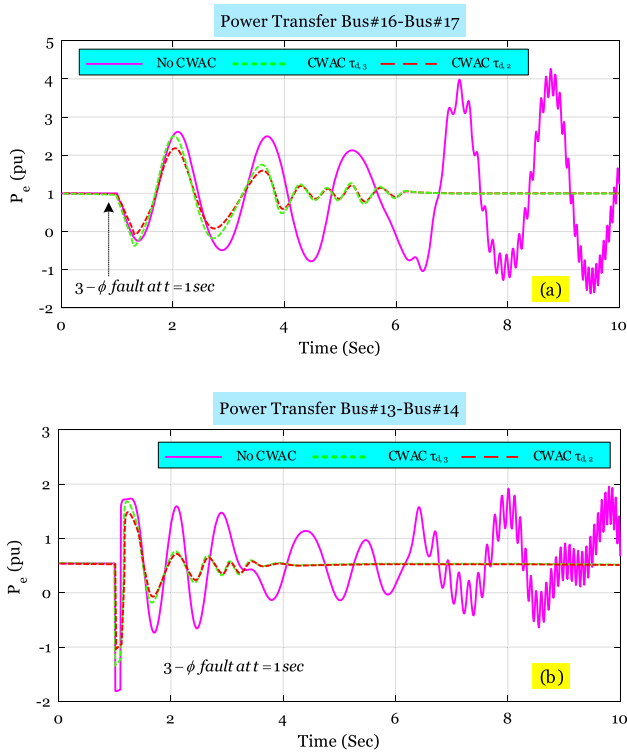
Fig. 21 Response of CWAC with $\tau_{d,2} = 0.2$ sec, and $\tau_{d,3} = 0.5$ sec, **a** transfer power (P_e) bus#16-bus#17 in pu; **b** transfer power (P_e) bus#13-bus#14 in pu

effectively and the oscillation settles down within 2 s. The oscillation's settling period for the active power variation is also acceptable.

The CWAC's performances under consideration of large transmission delays and faulty conditions are shown in Fig. 21. When a $\tau_{d,3} = 0.5$ sec delay in the wide area signal is taken into account, it can be seen from Fig. 21 that the controllers offer enough damping to end the oscillation in 2 s. The effectiveness of the suggested CWAC is then verified for local area modes. However, when delays longer than one second are taken into account in the control loop, the damping performance of the CWAC for local area mode is drastically reduced. As a result, the oscillation takes longer to stop and has a longer settling time. When modest transmission delays are taken into account in wide-area signals, the performance of the CWAC is seen in Fig. 19 through 21. The performance of the CWAC on the local modes is essentially identical to both normal conditions and defective environment.

The responses with CWAC in terms of rotor speed deviations are shown in Fig. 22 when various time delays and perturbations are taken into account. The speed difference $\Delta\omega_r$ between generators G_5 and G_1 is shown in Fig. 22a with delays $\tau_{d,2} = 0.2$ sec, $\tau_{d,3} = 0.5$ sec, and 3-φ fault. The speed difference $\Delta\omega_r$ between generators G_6 and G_6, and G_1 is shown in Fig. 22b. The speed difference $\Delta\omega_r$ between
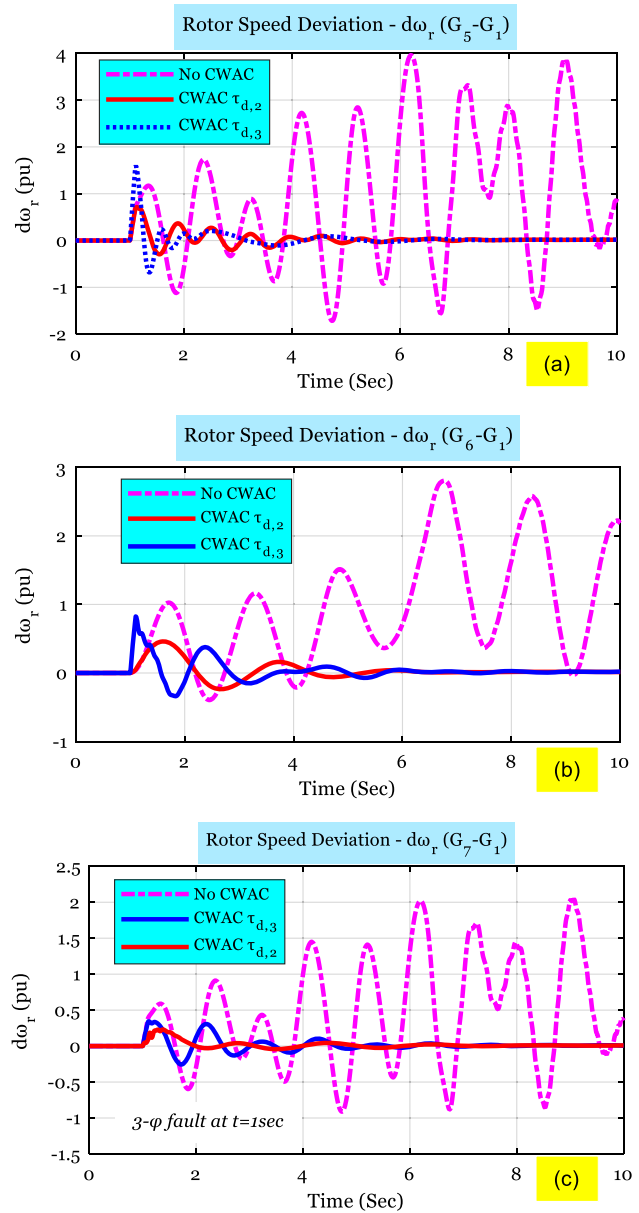

Fig. 22 Response of CWAC with $\tau_{d,2} = 0.2$ sec, and $\tau_{d,3} = 0.5$ sec, **a** rotor speed deviation ($\Delta\omega_r$) $G_5 - G_1$ in pu; **b** $\Delta\omega_r$ $G_6 - G_1$ in pu; **c** $\Delta\omega_r$ $G_7 - G_1$ in pu

generators G_7 and G_1 is shown in Fig. 22c. The system is unstable in no CWAC case after the disturbance, however in the CWAC case, the system is back to being stable after the disturbance in a matter of milliseconds. The comparative damping considering different time delays are given in Table 4. Overall, the simulation results indicate that CWAC can provide LFO IAO modes with enough damping.

Table 4 Comparative results of CWAC with different time delays

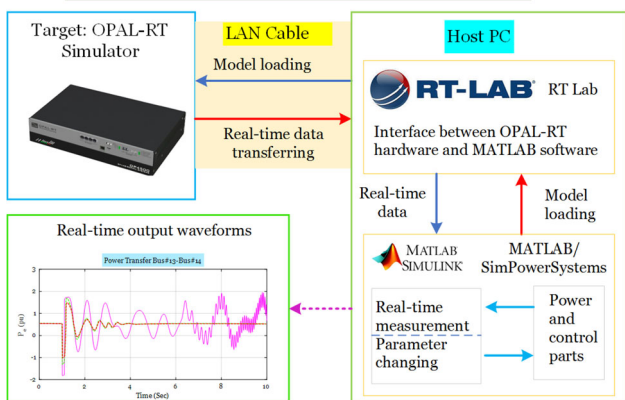| CWAC (delay − sec) ↓	Mode #1		Mode #2		Mode #3	
	$f(Hz)$	ξ	$f(Hz)$	ξ	$f(Hz)$	ξ
$\tau_{d,1} = 0$ s	0.4963	0.7654	0.5473	0.9321	0.8962	0.8985
$\tau_{d,2} = 0.2$ s	0.3021	0.6964	0.3629	0.7514	0.5334	0.7754
$\tau_{d,3} = 0.5$ s	0.4692	0.6031	0.6329	0.7106	0.4988	0.6755
$\tau_{d,4} = 0.75$ s	0.5318	0.4651	0.5234	0.3629	0.6344	0.3193

Fig. 23 Real-time experiment setup. 1—Digital oscilloscope; 2—Host PC with RT-LAB and MATLAB; 3—OP4500 simulator, and OPAL-RT digital simulator in the real-time simulation process
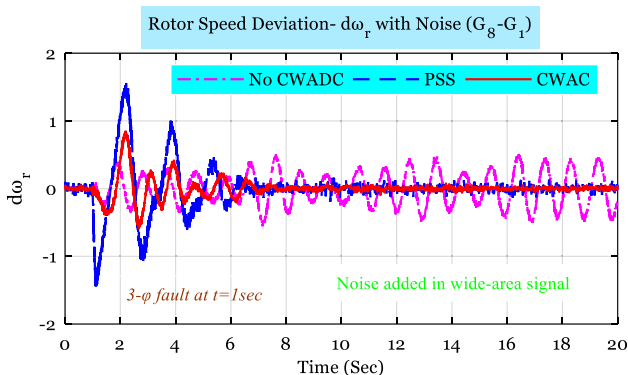

Fig. 24 Response of CWAC with noise, $\Delta\omega_r$ $G_8 - G_1$ in pu

6.2 OPAL-RT Simulator

The real-time simulator is interfaced with MATLAB/Simulink models to enable performance verification of the proposed CWAC controllers. Real-time verification of the MATLAB simulation results is required for the performance validation of the suggested CWAC. The numerical off-line simulations in MATLAB produce precise results. The time responses of the numerical simulations, however, are slower than those of the real systems for big systems. Unfortunately, it is exceedingly difficult and economically unfeasible for academic or industrial reasons to construct big and complex systems in real-time, such as power systems. Real-time simulators, which leverage parallel computing resources to execute the simulation in real-time and give the user the results exactly as they occur in the real system, are used to solve the aforementioned issue.

In this study, high-end Intel multi-core CPUs are combined with the Xilinx Kintex 7 FPGA MMPK7 board to run real time simulations in the OP4500 real-time digital simulator. OPAL-RT, Ontario, Canada, is the producer of the real-time digital simulator OP4500. Two main tools make up the real-time digital simulator OP4500: a real-time distributed simulation package (RT-LAB) and algorithmic toolboxes for running Simulink block graphs on a desktop computer and simulating power networks and their controllers in appointed-time efforts, respectively. RT-LAB is composed mostly of two components. One is the host computer, which provides a user interface and modifies the Simulink model before RT-LAB generates it. Another option is the RT simulator, which uses the REDHAT operating system to execute real-time models and offers telnet connectivity with the host computer. The RT-LAB offers a distributed real-time environment with high accuracy, low cost, and tiny time steps for the MATLAB/Simulink models to closely imitate the real power system.

Using the OPAL-RT real-time simulator and various operating scenarios, the modified RESs incorporated NETS power system's real-time performance and robustness are evaluated. As seen in Fig. 23, the experimental setup for the OPAL-RT OP4500 real-time simulator comprises a host computer, a target PC (OP4500), and a digital oscilloscope.

In the SimPowerSystems environment, real-time waveforms can be measured after model loading and real time data obtaining.

Furthermore, to evaluate the capability of the suggested CWAC while taking into account faulty communication, such as noise in wide area signals. Modern power systems with phasor measuring units (PMUs) are used to create an efficient CWAC. At a sampling rate of 5–60 Hz, PMUs intelligently record data from synchronized electrical systems using the GPS; nevertheless, these data invariably contain noise [49]–[50]. In order to achieve this, feedback signals and noise are combined. The signal-to-noise ratio (SNR), which is measured in decibels (dB) from the standard deviation, is used to describe how often noise degrades wide area signals.

As shown in Fig. 2, and Fig. 12, the CWAC requires the rotor speed deviations as input; hence, the generator speed readings are routed through a washout filter. In order to avoid interfering with the study frequency range (0.3–1.8 Hz), a washout block with a time constant of 6 s is employed. Fig. 24 displays the rotor speed variances after a disturbance happens at time t = 1 s. It is advantageous to use local measurements alone for the filtering since the waveforms showed that the disturbance does not start at every site instantly but exhibits a propagation delay that is nonzero.

The responses of CWAC to noise presents in control signal in terms of the rotor speed variances $\Delta\omega_r$ between generators G_8 and G_1 is shown in Fig. 24. Figure 24 shows what happens when no control measures are used to stabilize the system after a significant disturbance: the rotor speed oscillations increase. In scenario-7, noise is taken into account, with a 3-φ fault is introduced at $t = 1$ sec between buses #16 and #17 with a fault period of $100\,m$ sec. These simulated results show that the advised CWAC efficiently mitigates IAOs. Oscillations stop using the suggested CWAC in less than 4 s, which is acceptable.

In conclusion, the proposed CWAC significantly reduces LFOs caused by renewable converters and significant disturbances in large integrated renewable systems. Reduce the impact of time delay and noise that occurs in wide area communications as well.

7 Conclusions

In order to increase the damping for LFO IAO modes, while also taking into consideration the renewable converters and communication procrastination, this research provides a new coordinated design of a wide-area control system with CIGs. An introduction to the classification of power system stability and an examination of the various types of oscillation modes prevalent in power systems served as the foundation for the study project. In essence, LDCs like speed and power input-based PSSs suppress local oscillation modes. However, for LFO IAO modes, the LDCs do not offer enough dampening. Therefore, it is suggested that you use a CWAC to damp out these LFOs. The current interconnected power system networks are wide and display dynamic behavior that is highly nonlinear. To ensure the system's safe and reliable operation, it is necessary to maintain the system's reliability with an acceptable margin. The instability phenomenon found in the power system are categorized as stability of voltage, the stability of speed, and stability of the rotor angle. The stability of the rotor angle is often defined as transient stability and small signal stability. The stability of the small signal rotor angle was examined by conducting the eigenvalue analysis over the linearized system model, whereas the transient stability was estimated by using simulations of the time domain.

In order to confirm the efficacy of the suggested CWAC, a modified NETS power system is taken into consideration as a case study. Using MATLAB/Simulink, the case study's small signal assessment and nonlinear time domain simulation studies are completed under various operating situations. According to the results of the simulation, the suggested CWAC will adequately dampen the IAOs in the presence of time delays and noise. Additionally, the proposed CWAC's performance is assessed using the real-time digital simulator OPAL-RT. The simulation results using MATLAB/Simulink and the real-time OPAL-RT show that the proposed CWAC improves the dynamic performance of the power system under various operating situations and provides enough damping to the IAOs. The acquired data lead to the conclusion that the suggested CWAC strategy performs better than the LDCs.

The following areas are suggested for immediate future examination as an extension of the work now being done, based on the research given in this paper. By using a communication network for feedback, new issues including time delays, packet dropouts, and packet disordering are created. Only time delays are taken into account when designing the CWAC in this paper. Constraints on the communication network must also be taken into account when designing the CWAC. The proposed control approach can be also validated on real-time large power systems by incorporating more penetration of renewable and energy storage devices.

Declarations

Conflict of interest The author declares that they have no known competing financial interests or personal relationships that could have appeared to influence the work reported in this paper.

Appendix

Table 5 provides the eigenvalues of the linearized reduced order modified NETS system.

Table 5 Small-signal analysis of NETS, eigenvalues of linearized reduced order system

S.no	Eigenvalues $(\lambda = \rho \pm j\omega)$	Frequency (Hz)	Dampling $(\zeta\ in\ \%)$	S.no	Eigenvalues $(\lambda = \rho \pm j\omega)$	Frequency (Hz)	Dampling $(\zeta\ in\ \%)$
1	$-0.4505 + j0.6750$	0.107	-55.514	30	$-65.165 + j0.0$	0.0	100.0
2	$-0.4861 + j0.6278$	0.100	-61.222	31	$-64.250 + j0.0$	0.0	100.0
3	$-0.4812 + j0.6084$	0.097	-62.035	32	$-63.948 + j0.0$	0.0	100.0
4	$-0.6901 + j0.8108$	0.129	64.813	33	$-65.797 + j0.0$	0.0	100.0
5	$-0.5780 + j0.6705$	0.107	-65.293	34	$-65.936 + j0.0$	0.0	100.0
6	$-0.7928 + j0.8127$	0.129	-69.831	35	$-63.535 + j0.0$	0.0	100.0
7	$-4.4830 + j4.1880$	0.666	73.074	36	$-61.774 + j0.0$	0.0	100.0
8	$-0.8648 + j0.7743$	0.123	74.505	37	$-65.936 + j0.0$	0.0	100.0
9	$-2.9562 + j2.5076$	0.399	76.260	38	$-59.612 + j0.0$	0.0	100.0
10	$-2.0436 + j1.6338$	0.260	78.107	39	$-32.118 + j0.0$	0.0	100.0
11	$-1.2040 + j0.9107$	0.145	79.755	40	$-13.988 + j0.0$	0.0	100.0
12	$-4.3350 + j2.9883$	0.475	82.333	41	$-7.3691 + j0.0$	0.0	100.0
13	$-5.7301 + j3.6713$	0.584	84.200	42	$-7.1480 + j0.0$	0.0	100.0
14	$-12.618 + j6.6283$	1.055	88.528	43	$-5.8943 + j0.0$	0.0	100.0
15	$1.4761 + j0.5231$	0.083	94.256	44	$-5.5374 + j0.0$	0.0	100.0
16	$-4.3697 + j1.5310$	0.244	94.375	45	$-2.8327 + j0.0$	0.0	100.0
17	$-1.0444 + j0.2387$	0.038	97.486	46	$-2.0263 + j0.0$	0.0	100.0
18	$-19.993 + j1.2699$	0.202	99.799	47	$-1.5315 + j0.0$	0.0	100.0
19	$-104.59 + j0.0$	0.0	100.0	48	$-1.4500 + j0.0$	0.0	100.0
20	$-103.78 + j0.0$	0.0	100.0	49	$-1.0995 + j0.0$	0.0	100.0
21	$-102.68 + j0.0$	0.0	100.0	50	$-0.9758 + j0.0$	0.0	100.0
22	$-102.27 + j0.0$	0.0	100.0	51	$-0.9592 + j0.0$	0.0	100.0
23	$-102.13 + j0.0$	0.0	100.0	52	$-0.9066 + j0.0$	0.0	100.0
24	$-101.90 + j0.0$	0.0	100.0	53	$-0.1920 + j0.0$	0.0	100.0
25	$-101.33 + j0.0$	0.0	100.0	54	$-0.1007 + j0.0$	0.0	100.0
26	$-101.32 + j0.0$	0.0	100.0	55	$-0.1003 + j0.0$	0.0	100.0
27	$-101.31 + j0.0$	0.0	100.0	56	$-0.1002 + j0.0$	0.0	100.0
28	$-100.90 + j0.0$	0.0	100.0	57	$-72.869 + j0.0$	0.0	100.0
29	$-65.987 + j0.0$	0.0	100.0				

References

1. Kunjumuhammed, L.; Kuenzel, S.; Pal, B.: "Simulation of power system with renewables," Acad. Press, ISBN 978-0-12-811187-1, 2020. https://doi.org/10.1016/C2016-0-00813-6

2. Hatziargyriou, N.; Milanović, J.V.; Rahmann, C.: Definition and classification of power system stability—revisited & extended. IEEE Trans. Power Syst. **36**(4), 3271–3281 (2021). https://doi.org/10.1109/TPWRS.2020.3041774

3. Pal, B.; Chaudhuri, B.: "Robust control in power systems," Power electronics and power systems, (Eds.) M. A. Pai and Alex Stankovic), ISBN 978-0387-25949-9, Springer US, (2005)

4. Adapa, R.; Feliachi, A.; Yang, X.: Damping enhancement in the Western u.s. power system: a case study. IEEE Trans. Power Syst. **10**(3), 1271–1278 (1995)

5. Kamwa, I.; Gérin-Lajoie, L.: State-space system identification-toward MIMO models for modal analysis and optimization of bulk power systems. IEEE Trans. Power Syst. **15**(1), 326–335 (2000)

6. Martins, N.; Barbosa, A.A.; Ferraz, J.C.R.; Dos Santos, M.G; Bergamo, A.L.B.; Yung, C.S.; Roliveira, V; MaCedo, N.J.P.: Retuning stabilizers for the north-south brazilian interconnection, 1999 IEEE power engineering society summer meeting, PES 1999—Conference Proceedings, 1, 58–67 (1999)

7. Liu, S.; Deng, H.; Guo, S.: Analyses and discussions of the blackout in indian power grid. Energy Sci. Technol. **6**, 61–66 (2013)

8. Haes Alhelou, H.; Hamedani-Golshan, M.E.; Njenda, T.C.; Siano, P.: A survey on power system blackout and cascading events: research motivations and challenges. Energies **12**(4), 682 (2019)

9. Prasertwong, K.; Mithulananthan, N.; Thakur, D.: 'Understanding low-frequency oscillation in power systems.' Int. J. Electr. Eng. Educ. **47**(3), 248–262 (2010)

10. Rogers, G.: Power system oscillations. Springer science & business media (2012)

11. Rouco, L.; Pagola, F. L.: "Eigenvalue sensitivities for design of power system damping controllers," Proceedings of the 40th IEEE Conference on decision and control (Cat. No.01CH37228), Orlando, FL, USA, vol.4, pp. 3051–3055 (2001)

12. Deng, J.; Li, C.; Zhang, X.-P.: Coordinated design of multiple robust facts damping controllers: a BMI-based sequential approach with multi-model systems. IEEE Trans. Power Syst. **30**(6), 3150–3159 (2015). https://doi.org/10.1109/TPWRS.2015.2392153

13. Larsen, E.V.; Swann, D.A.: Applying power system stabilizers part I: general concepts. IEEE Trans. Power Appar. Syst. **6**, 3017–3024 (1981)

14. Wong, D.Y.; Rogers, G.J.; Porretta, B.; Kundur, P.: Eigenvalue analysis of very large power systems. IEEE Trans. Power Syst. **3**(2), 472–480 (1988)

15. Klein, M.; Le, L.X.; Rogers, G.J.; Farrokhpay, S.; Balu, N.J.: H/sub/spl infin damping controller design in large power systems. IEEE Trans. Power Syst. **10**(1), 158–166 (1995)

16. Scherer, C.; Gahinet, P.; Chilali, M.: Multiobjective output-feedback control via LMI optimization. IEEE Trans. Autom. Control **42**(7), 896–911 (1997)

17. Rao, P.S.; Sen, I.: Robust pole placement stabilizer design using linear matrix inequalities. IEEE Trans. Power Syst. **15**(1), 313–319 (2000)

18. Yao, W.; Jiang, L.; Wen, J.; Wu, Q.; Cheng, S.: 'Wide-area damping controller for power system inter-area oscillations: a networked predictive control approach.' IEEE Trans. Control Syst. Technol. **23**(1), 27–36 (2015)

19. Zhang, Y.; Bose, A.: 'Design of wide-area damping controllers for inter-area oscillations.' IEEE Trans. Power Syst. **23**(3), 1136–1143 (2008)

20. Yang, N.; Liu, Q.; McCalley, J.D.: 'TCSC controller design for damping interarea oscillations.' IEEE Trans. Power Syst. **13**(4), 1304–1310 (1998)

21. Zarghami, M.; Crow, M.L.; Sarangapani, J.; Liu, Y.; Atcitty, S.: 'A novel approach to interarea oscillation damping by unified power flow controllers utilizing ultracapacitors.' IEEE Trans. Power Syst. **25**(1), 404–412 (2010)

22. Deng, J.; Li, C.; Zhang, X.-P.: 'Coordinated design of multiple robust FACTS damping controllers: a bmi-based sequential approach with multi-model systems.' IEEE Trans. Power Syst. **30**(6), 3150–3159 (2015)

23. Li, Y.; Rehtanz, C.; Ruberg, S.; Luo, L.; Cao, Y.: 'Wide-area robust coordination approach of HVDC and FACTS controllers for damping multiple interarea oscillations.' IEEE Trans. Power Deliv. **27**(3), 1096–1105 (2012)

24. Lu, C.; Wu, X.; Wu, J.; Li, P.; Han, Y.; Li, L.: "Implementations and experiences of wide-area HVDC damping control in china southern power grid," in power and energy society general meeting, 2012 IEEE. IEEE, pp. 1–7 (2012)

25. Juanjuan, W.; Chuang, F.; Yao, Z.: 'Design of WAMS-based multiple HVDC damping control system.' IEEE Trans. Smart Grid **2**(2), 363–374 (2011)

26. Radwan, M.M.; Azmy, A.M.; Ali, G.E.; ELGebaly, A.E.: Optimal design and control loop selection for a STATCOM wide-area damping controller considering communication time delays. Int. J. Electr. Power Energy Syst. **149**, 109056 (2023)

27. Bento, M.E.: Resilient wide-area damping controller design using crow search algorithm. IFAC-PapersOnLine **55**(1), 938–943 (2022)

28. Darabian, M.; Bagheri, A.: Design of adaptive wide-area damping controller based on delay scheduling for improving small-signal oscillations. Int. J. Electr. Power Energy Syst. **133**, 107224 (2021)

29. Bento, M.E.C.: A hybrid particle swarm optimization algorithm for the wide-area damping control design. IEEE Trans. Industr. Inf. **18**(1), 592–599 (2022)

30. Ranjbar, S.: STATCOM-based intelligent wide-area controller for damping interarea oscillation. IEEE Syst. J. **17**(3), 4062–4069 (2023)

31. Isbeih, Y.J.; Ghosh, S.; Moursi, M.S.E.; El-Saadany, E.F.: Online DMDc based model identification approach for transient stability enhancement using wide area measurements. IEEE Trans. Power Syst. **36**(5), 4884–4887 (2021)

32. Qi, J.; Wu, Q.; Zhang, Y.; Weng, G.; Zhou, D.: Unified residue method for design of compact wide-area damping controller based on power system stabilizer. J. Modern Power Syst. Clean Energy **8**(2), 367–376 (2020)

33. Kumar, K.; Prakash, A.; Singh, P.; Parida, S.K.: Large-scale solar PV converter based robust wide-area damping controller for critical low frequency oscillations in power systems. IEEE Trans. Ind. Appl. **59**(4), 4868–4879 (2023)

34. Pradhan, V.; Kulkarni, A.M.; Khaparde, S.A.: A model-free approach for emergency damping control using wide area measurements. IEEE Trans. Power Syst. **33**(5), 4902–4912 (2018)

35. Sengupta, A.; Das, D.K.; Subudhi, B.: A delay-dependent dynamic wide area damping controller for renewable energy integrated power system resilient to communication failure. CSEE J. Power Energy Syst. **9**(2), 577–588 (2023)

36. Ian Hiskens, "IEEE PES task force on benchmark systems for small-signal stability analysis and control," Technical report PES-TR18, IEEE Power & Energy Society, November 19, 2013. Available: http://www1.sel.eesc.usp.br/ieee/

37. IEEE PES Task Force on Benchmark Systems for Small-Signal Stability Analysis and Control, Technical Report PES-TR18, IEEE Power & Energy Society, Aug, 2015. Available: http://www1.sel.eesc.usp.br/ieee/

38. Model user guide for generic renewable energy system models. EPRI, Palo Alto, CA: 2018. 3002014083.

39. WECC solar photovoltaic power plant modeling and validation guideline MVWG december 9, 2019. Available: https://www.wecc.org/Reliability/Solar%20PV%20Plant%20Modeling%20and%20Validation%20Guidline.pdf

40. Catalán, P.; Wang, Y.; Arza, J.; Chen, Z.: A comprehensive overview of power converter applied in high-power wind turbine: key challenges and potential solutions. IEEE Trans. Power Electron. **38**(5), 6169–6195 (2023)

41. Yang, M.; Zhang, L.; Cui, Y.; Zhou, Y.; Chen, Y.; Yan, G.: Investigating the wind power smoothing effect using set pair analysis. IEEE Trans. Sustain. Energy **11**(3), 1161–1172 (2020)

42. Ge, X.; Qian, J.; Fu, Y.; Lee, W.-J.; Mi, Y.: Transient stability evaluation criterion of multi-wind farms integrated power system. IEEE Trans. Power Syst. **37**(4), 3137–3140 (2022)

43. Jiang, S.; Xu, Y.; Li, G.; Xin, Y.; Wang, L.: Coordinated control strategy of receiving-end fault ride-through for DC grid connected large-scale wind power. IEEE Trans. Power Delivery **37**(4), 2673–2683 (2022)

44. Rahman, S., et al.: Analysis of power grid voltage stability with high penetration of solar PV systems. IEEE Trans. Ind. Appl. **57**(3), 2245–2257 (2021)

45. Bothwell, C.D.; Hobbs, B.F.: How sampling and averaging historical solar and wind data can distort resource adequacy. IEEE Trans. Sustain. Energy **14**(3), 1337–1345 (2023)

46. Wu, Z.; Zhou, M.; Wang, J.; Du, E.; Zhang, N.; Li, G.: Profit-sharing mechanism for aggregation of wind farms and concentrating solar power. IEEE Trans. Sustain. Energy **11**(4), 2606–2616 (2020)

47. Chen, B., et al.: Distributionally robust coordinated expansion planning for generation, transmission, and demand side resources considering the benefits of concentrating solar power plants. IEEE Trans. Power Syst. **38**(2), 1205–1218 (2023)

48. Mir, A.S.; Senroy, N.: DFIG damping controller design using robust CKF-based adaptive dynamic programming. IEEE Trans. Sustain. Energy **11**(2), 839–850 (2020)

49. Zhao, Y., et al.: Resilient adaptive wide-area damping control to mitigate false data injection attacks. IEEE Syst. J. **15**(4), 4831–4842 (2021)

50. Zenelis, I.; Wang, X.; Kamwa, I.: Online PMU-based wide-area damping control for multiple inter-area modes. IEEE Trans. Smart Grid **11**(6), 5451–5461 (2020)